

Article

Crystal Growth, Photoluminescence and Radioluminescence Properties of Ce³⁺-Doped Ba₃Y(PO₄)₃ Crystal

Zhenggang Zou^{1,2}, Jiaolin Weng³, Chun Liu¹, Yiyang Lin¹, Jiawei Zhu¹, Yijian Sun^{1,2} , Jianhui Huang⁴, Guoliang Gong^{1,2,4,*} and Herui Wen^{1,2,*}

- ¹ Jiangxi Provincial Key Laboratory of Functional Crystalline Materials Chemistry, School of Chemistry and Chemical Engineering, Jiangxi University of Science and Technology, Ganzhou 341000, China; zouzhenggang15@163.com (Z.Z.); lc614560232@163.com (C.L.); linyiyang9817@163.com (Y.L.); zjw915639659@163.com (J.Z.); sunyijian@jxust.edu.cn (Y.S.)
- ² National Rare Earth Functional Material Innovation Center, Ganzhou 341000, China
- ³ College of Material Engineering, Fujian Agriculture and Forestry University, Fuzhou 350108, China; 15060317686@163.com
- ⁴ College of Rare Earths, Jiangxi University of Science and Technology, Ganzhou 341000, China; huangjianhui@jxust.edu.cn
- * Correspondence: gonggl@jxust.edu.cn (G.G.); wenherui63@163.com (H.W.)

Abstract: Inorganic scintillation crystals have been widely used in applications of high-energy physics, nuclear medical imaging, industrial nondestructive inspection, etc. In this work, a single crystal Ba₃Y(PO₄)₃ (BYP) with 1.0 at% Ce³⁺-doping concentration was first grown by the Czochralski method, and the electronic structure was calculated using first principles based on density functional theory. In addition, a series of Ce³⁺-doped BYP phosphors were synthesized, and the fluorescence emission under UV excitation was measured through low-temperature spectroscopy, containing double-peaked emission from 5d–4f transition and self-trapped exciton recombination. A comparison of the UV and X-ray-excited fluorescence spectra reveals the existence of oxygen vacancies as well as F⁺ centers in the crystal. The air annealing of the crystal effectively reduces the thermoluminescence defects but reduces the emission intensity under UV or X-ray excitation. The BYP:Ce crystal shows a fast decay lifetime of 15.5 ns, and the fast component is as short as 8 ns. The results show that the Ce³⁺-doped BYP crystal has potential as a kind of scintillator with fast decay properties.

Keywords: Ba₃Y(PO₄)₃ crystal growth; Ce³⁺-doped; scintillation; radioluminescence



Citation: Zou, Z.; Weng, J.; Liu, C.; Lin, Y.; Zhu, J.; Sun, Y.; Huang, J.; Gong, G.; Wen, H. Crystal Growth, Photoluminescence and Radioluminescence Properties of Ce³⁺-Doped Ba₃Y(PO₄)₃ Crystal. *Crystals* **2024**, *14*, 431. <https://doi.org/10.3390/cryst14050431>

Academic Editor: Vladimir M. Kaganer

Received: 10 April 2024

Revised: 27 April 2024

Accepted: 29 April 2024

Published: 30 April 2024



Copyright: © 2024 by the authors. Licensee MDPI, Basel, Switzerland. This article is an open access article distributed under the terms and conditions of the Creative Commons Attribution (CC BY) license (<https://creativecommons.org/licenses/by/4.0/>).

1. Introduction

Inorganic scintillation materials that convert high-energy rays or particles into large amounts of low-energy photons have been extensively used in radiation detection fields, such as nuclear medical diagnosis, security systems, high-energy physics and well logging [1–6]. When the ionizing radiation is absorbed, the photoelectric effect (<10² keV), the electron pair effect (10² keV–8 MeV), and the Compton effect (>8 MeV) occur separately or in steps according to the energy of the incident photon, thereby converting the high-energy photon into secondary charged particles and simultaneously generating thermalized electron–hole pairs with a forbidden bandwidth energy of approximately E_g. Subsequently, electrons and holes transfer energy to the luminescent centers close to the conduction and valence bands by means of in-band transitions and electron–phonon relaxation, respectively; finally, the excited state electrons in the luminescent center return to the ground state, accomplished by emitting photons or non-radiation transitions [7]. However, scintillation materials often have certain amounts of lattice defects and dislocations, leading to the presence of defect energy levels in the forbidden bands of the materials. The recombination of electrons and holes competes with the trapping of defect states [8]. The trapped electrons can return to the conduction band through thermal activation [9]. Furthermore, more unexpected self-trapped excitons

(STEs) can be generated and further dissipated through relaxing due to defects or involving the lattice vibration, resulting in non-radiative recombination [10]. The performance of the scintillator is adversely impacted by these processes [11].

The development of Ce^{3+} -activated inorganic scintillator crystals continues to show unique attraction due to their high light output, fast decay lifetime to tens of nanoseconds, and emissive wavelength typically located in the ultraviolet or visible spectral ranges [12–14]. The rare-earth aluminate and silicate oxide scintillators have attracted much attention over the last two decades, with the advancement of commercially available Ce-activated oxide scintillators, such as the GGAG, YAP, Gd_2SiO_5 , and $(\text{Lu},\text{Y})_2\text{SiO}_5$ crystals, which are characterized by high optical yields ($>20,000$ phonons/MeV), easier large-size growth, and outstanding irradiation resistance. However, there are few reports on the scintillation properties of phosphate crystals so far, which is mainly due to the scarcity of rare-earth phosphate crystals with stable physical and chemical properties and easy growth. Specifically, the average melting points of the series REPO_4 crystals are extremely high (>2000 °C), and the volatilization of the P components is so severe that it is difficult to obtain high-quality single crystals.

Recently, orthophosphate crystals $\text{M}_3\text{RE}(\text{PO}_4)_3$ (RE: rare earths, lanthanides; M: Sr or Ba) with cationic disordered structure have sparked widespread concern based on their outstanding optical properties [15–18]. $\text{Ba}_3\text{Y}(\text{PO}_4)_3$ (BYP) belongs to the eulytite-type compounds, which have considerable physical and chemical stability, a large band gap (>6 eV), and good doping capacity for rare-earth ions [19,20]. In the last few years, a large number of studies based on the BYP matrix have focused on the tunable visible phosphors doped with rare-earth ions like Eu^{3+} , Dy^{3+} , Sm^{3+} , etc., or temperature-sensing phosphors with $\text{Ce}^{3+}/\text{Eu}^{2+}/\text{Mn}^{2+}$, $\text{Ce}^{3+}/\text{Tb}^{3+}$, $\text{Tb}^{3+}/\text{Eu}^{3+}$ ions, etc. [21–26]. Y. Takebuchi et al. have reported that the $\text{Ba}_3\text{RE}(\text{PO}_4)_3$ (RE = Y, La and Lu) crystals showed the intrinsic luminescence peaked at 400 nm under vacuum-UV and X-ray excitation; the X-ray-induced scintillation decay time was several microseconds, and the absolute light yields were estimated to be 960, 1160, and 1220 ph/5.5 MeV under ^{241}Am α -ray irradiation, respectively [27]. H. Ezawa et al. have reported that the undoped and Tb-doped BYP crystals exhibited the STEs and 4f–4f transitions of Tb^{3+} luminescence, respectively, and the thermally stimulated luminescence was observable from 0.01 mGy in 1% Tb-doped BYP [28]. In recent years, the BYP crystal has been successfully grown by the Czochralski method at a temperature of about 1800 °C. However, the growth and properties of the Ce^{3+} -doped BYP crystal have never been investigated.

In this work, a single crystal of $\text{Ba}_3\text{Y}(\text{PO}_4)_3$ doped with $x = 0.01$ Ce^{3+} was first grown by the Czochralski method, the crystal structure was analyzed, and the electronic band structure was calculated. The photoluminescence properties of $\text{BYP}:\text{xCe}^{3+}$ powder samples were investigated in detail. The radioluminescence properties of $\text{BYP}:\text{Ce}^{3+}$ crystals before and after air-annealed treatment were measured and discussed, which provides a meaningful method for the further development of phosphate crystals for scintillator applications.

2. Experiment

2.1. Experimental Details

Since the disordered occupancy of Ba^{2+} and Y^{3+} ions in BYP lattices has been reported, we chose Ce^{3+} to replace Y^{3+} for doping based on the similarity of valence, electronegativity, and ion radius. A $\text{BYP}:\text{Ce}^{3+}$ single crystal was grown by the Czochralski method with $x = 0.01$ Ce^{3+} -doping ratio. The raw materials, including CeO_2 and Y_2O_3 with 99.99% purity, and $\text{NH}_4\text{H}_2\text{PO}_4$ and BaCO_3 with AR purity, were purchased from Aladdin's Reagent, Inc. During the sintering of powder samples and crystal growth, NH_4HPO_4 was added in excess of 5% due to the serious volatilization at high temperatures. The phosphors of $\text{BYP}:\text{xCe}^{3+}$ with Ce^{3+} -doping concentrations of $x = 0.005\text{--}0.07$ were prepared by the high-temperature solid-state reaction. After being mixed evenly in the mortar, compressing into pellets, and subsequently sintering at 1300 °C for 10–20 h, the powder of $\text{BYP}:\text{xCe}^{3+}$ samples was obtained after annealing with the furnace.

The BYP:0.01Ce³⁺ powder sample was pressed onto several plates and loaded into a Φ 50 mm iridium crucible for crystal growth under high-purity nitrogen. For first-time crystal growth, an iridium rod was used as the seed and subsequently utilized for next-time crystal growth. During the growth process, the pulling speed was set to be 1–2 mm/h and the rotation speed was 10–12 rpm/min, respectively. In order to reduce the thermal stress and prevent crystal cracking, the slow process of cooling from 1800 °C to room temperature was set to 120 h. Ultimately, a colorless BYP:Ce³⁺ single crystal with Φ 20 × 15 mm³ and good optical quality was obtained.

The structural data of the BYP:Ce³⁺ were identified by single-crystal diffraction (Bruker D8 QUEST diffractometer, Bruker, Karlsruhe, Germany) and powder X-ray diffraction (PXRD, Rigaku Miniflex 600 diffractometer, Rigaku, Tokyo, Japan). The PXRD patterns of 2θ were collected in the range from 20 to 90° with a scanning speed of 8 °/min. The morphology and element distribution of the crystal were characterized using a field emission scanning electron microscope (FE-SEM, FEI MLA650F, FEI, Hillsboro, OR, USA), and the energy-dispersive spectrometer (EDS) was operated at 25 keV. The dimensions of 5 × 5 × 3 mm³ and 5 × 5 × 1 mm³ crystal wafers were processed for photoluminescence (PL) and thermoluminescence (TL) measurements, respectively. The concentration of Ce³⁺ in the BYP:Ce³⁺ crystal was determined by inductively coupled plasma atomic emission spectrometry (ICP-AES, TPS-7000, Puxi, Beijing, China). The fluorescence spectrometer (FLS980, Edinburgh Instruments Ltd., Livingston, UK) was employed to measure the fluorescence spectra and decay curve. All the tests were recorded at room temperature, except for the fluorescence spectra of BYP:0.007Ce³⁺ powder from 10 K to room temperature (RT). The crystal defects were characterized by TL spectroscopy (LTTL-3DS spectrometer, Guangzhou Radiation Technology, Guangzhou, China), which was equipped with an X-ray tube. The crystal wafer was irradiated for 10 min at a radiation dose of 5 Gy and then heated from room temperature to 770 K at 2 K/min. X-ray photoelectron spectroscopy (XPS) was carried out in a PHI 5000 VersaProbe III (Ulvac-Phi, Chigasaki, Japan), with a base pressure around 6.7×10^{-8} Pa, and the X-ray source was equipped with an Al K α monochromatic ($h\nu = 1486.6$ eV).

2.2. Computational Details

The theoretical calculations were performed using the CASTEP code with the generalized gradient approximation (GGA) and the Perdew–Burke–Ernzerhof (PBE) in Materials Studio 2020 [29,30]. The PBE provides a good balance between computational cost and accuracy, which performs well in estimating energy gaps compared to local density approximation (LDA) functionals, especially for periodic systems [31,32]. The Ba(4d¹⁰5p⁶6s²), Y(4p⁶4d¹5s²), P(3s²3p³) and O(2s²2p⁴) were treated as valence electrons, and their interactions with the cores were described by the projected augmented wave (PAW) approach [33]. The atomic structures of the unit cell were fully optimized until the total energies and forces on the atoms were converged to 10^{−6} eV and 0.01 eV Å^{−1}. One k-point (Gamma) was used to sample the Brillouin zone, and the cutoff energy of the plane-wave basis was set to 571.4 eV.

3. Results and Discussion

3.1. Lattice and Electronic Band Structure of BYP:Ce³⁺ Crystal

The PXRD patterns of the as-grown BYP:Ce³⁺ crystal are shown in Figure 1a, and the inset shows a photo of the crystal after processing. The PXRD patterns match well with the diffraction peaks of the standard cards of Ba₃La(PO₄)₃ (JCPDS, No. 29-0175); no extra diffraction peaks verify its pure phase structure. Also, the as-grown crystal was measured to obtain the experimental single-crystal diffraction data. The projected polyhedral in the lattice cell are present in Figure 1b, and the corresponding crystal data and structure refinement for the BYP:Ce are shown in Table 1. The BYP:Ce³⁺ crystallizes in the space group $I\bar{4}3d$, with four formula units per unit cell. The Ba²⁺/Y³⁺ ions are reported to be disorderedly occupied and present a distorted local polyhedral structure with bond lengths in the range of 2.59–3.28 Å. The P⁵⁺ ions are at the centers of a distorted oxygen tetrahedron

with average P–O bonds of 1.457 Å. The lattice parameters for the BYP:Ce³⁺ crystal are estimated to be $a = 10.467$ Å, comparable to $a = 10.465$ Å with respect to pure BYP in the literature [19]. The result indicates that Ce³⁺ doping induces a small expansion in the lattice, which is consistent with the larger ionic radius of Ce³⁺ (1.15 Å) than Y³⁺ (1.04 Å). In the case of Ba and Y-disordered occupancy, Ce doping will experience a variety of low-symmetry crystal field (CF) environments with weak CF strengths. Also, the significant electronegativity difference of the surrounding cations (Ba²⁺ and Y³⁺) and PO₄ polyhedral with small radii and easy twisting along polyhedral vertices will undoubtedly promote polarization of CF around the centered Ce³⁺. The actual concentration of Ce³⁺ ions in the as-grown BYP:Ce³⁺ crystal was determined to be 0.56 at.% by ICP-AES. The segregation coefficient was calculated to be 0.56. The reason for the low segregation coefficient of Ce³⁺ in BYP crystals may originate from the fact that the phosphate melts have a high viscosity, which inhibits the diffusion of Ce³⁺.

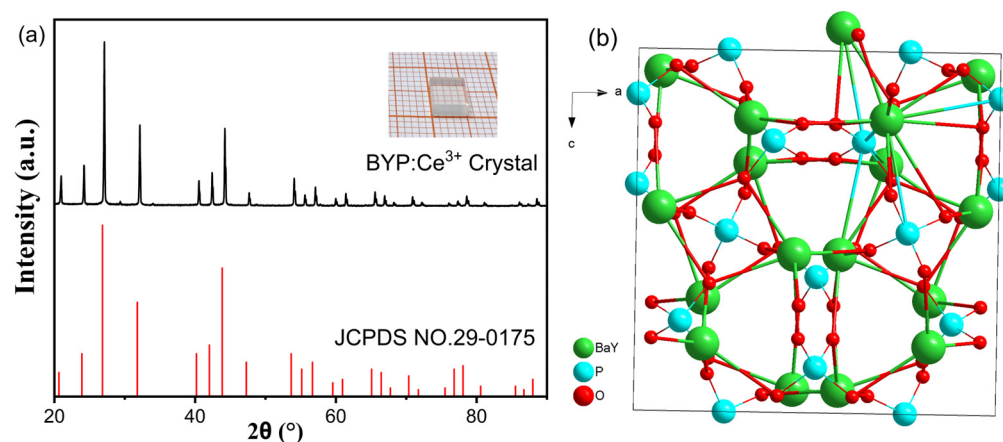


Figure 1. (a) The PXRD patterns and (b) unit cell of the BYP:0.01Ce³⁺ crystal.

Table 1. Crystal data and structure refinement for BYP:Ce³⁺.

Atom	x	y	z	U _{eq}
Ba1	0.68719(12)	0.81281(12)	0.18719(12)	0.0375(9)
Y1	0.68719(12)	0.81281(12)	0.18719(12)	0.0375(9)
P1	0.6250	0.5000	0.2500	0.0355(18)
O1	0.546(2)	0.604(2)	0.202(4)	0.172(16)

Note: Cell parameters: $a = b = c = 10.4665(6)$ Å, $\alpha = \beta = \gamma = 90^\circ$, $Z = 4$, $V = 1146.6(2)$ Å³; Space group: cubic, $I43d$ (220); Density: $\rho_{\text{calc}} = 4.552$ g/cm³. Reliability factors (R-factor): GOF = 1.065.

The FE-SEM image and EDS elemental mapping images of cerium, barium, yttrium, phosphorus and oxygen for the as-grown BYP:Ce crystal are shown in Figure 2. The lack of detail in the crystal surface process has no significant effect on the EDS results. Figure 2b–f clearly displays the different elements that are uniformly distributed inside the as-grown crystal. The Ce³⁺ doping concentration in the crystals is relatively low, but it can still be seen to be uniformly distributed inside the crystals, indicating that the crystals have a high degree of homogeneity.

The electronic band structure of the BYP:Ce³⁺ crystal was studied by density functional theory (DFT). Considering the low Ce³⁺-doping concentration ($x = 0.01$), and the small difference in lattice parameters of the Ce³⁺-doped BYP crystal compared to the undoped crystal reported in [19], we utilized the structure file of the above-analyzed BYP:Ce³⁺ crystal for the electronic structure calculations. The results of the calculated band structure of the BYP:Ce³⁺ crystal are shown in Figure 3a. The band structure of the crystal revealed that both the conduction band minimum (CBM) and valence band maximum (VBM) are located at the G high-symmetry point in the Brillouin zone. The BYP:Ce³⁺ crystal is a direct

bandgap insulator with an estimated bandgap of 5.324 eV. The projected density of states (PDOS) for the models of BYP is shown in Figure 3b. The PDOS reveals that the top of the VB is mainly composed of O-s/p, Y-s/p and Ba-p orbitals in the BYP crystal, with an additional feeble P-s/p orbital contribution. The bottom of the CB is mainly composed of Y-d and Ba-d orbitals. Y. Takebuchi et al. [27] reported that the undoped BREP crystals should have optical bandgaps exceeding 6.2 eV, while the $\text{Ba}_3\text{La}(\text{PO}_4)_3\text{:Ce}^{3+}$ phosphor is further clarified as having a bandgap of 7.21 eV [34]. The theoretically calculated bandgap value (5.324 eV) of BYP in this work is obviously low, which is even lower than the result deduced from the excitation spectra. We believe that the defects caused by the disordered occupancy of Ba and Y are the main influencing factors, which will inevitably affect the integrity and order of the local structure and promote site shifting of atoms due to the significant differences between Ba and Y in electronegativity and ionic radii, which in turn affects the theoretical calculations of DFT to a certain extent.

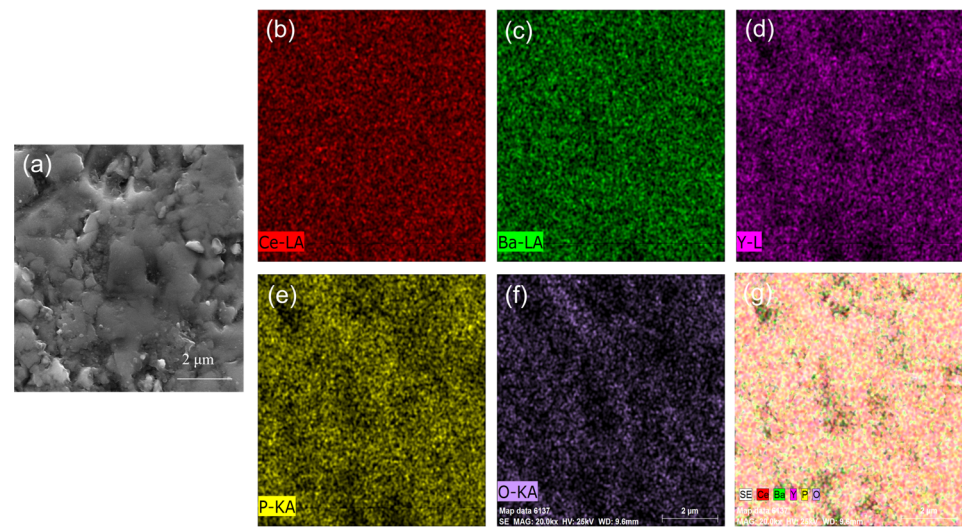


Figure 2. The FE-SEM image and EDS mapping images of the BYP:Ce^{3+} crystal: (a) FE-SEM image; (b–f) EDS mapping images for Ce, Ba, Y, P and O; and (g) overlay of the distribution of the (b–f), respectively.

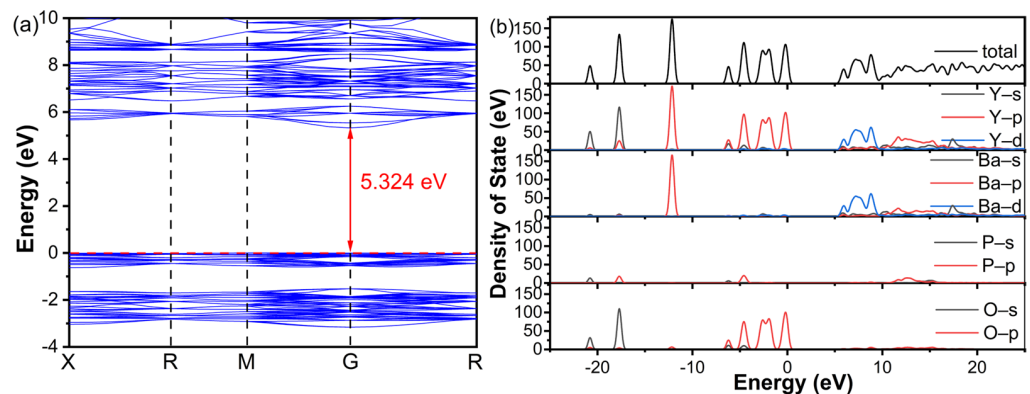


Figure 3. The calculated (a) band structure and (b) projected density of states of the BYP lattice.

3.2. Phase and PL Properties of the BYP:xCe^{3+} Phosphors

In order to determine the optimal doping concentration, we performed a simple screening of the Ce^{3+} doping concentrations in the form of a powder. The PXRD patterns of the BYP samples doped with gradient Ce^{3+} contents are shown in Figure 4. As can be seen, the diffraction peaks of the phosphors are consistent with those of the standard card (JCPDS No. 29-0175), indicating that all the synthesized phosphors are a unique pure phase and that the Ce^{3+} dopants have a negligible effect on the main phase structure.

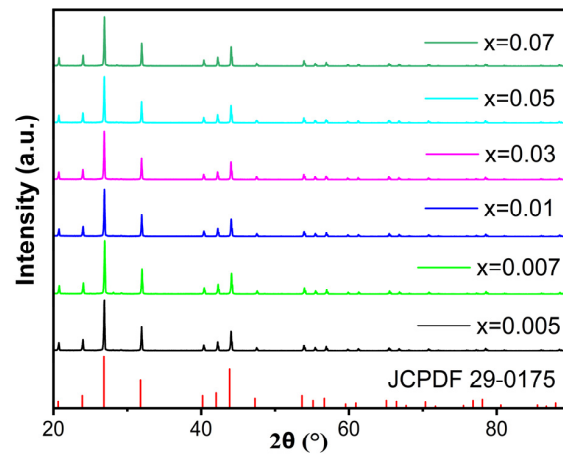


Figure 4. The PXRD patterns of the BYP: $x\text{Ce}^{3+}$ phosphors.

The PL spectra of BYP: $x\text{Ce}^{3+}$ phosphors are presented in Figure 5a, and the inset depicts the dependence of the Ce^{3+} doping concentration on the emission peak position and intensity. The emission intensity of BYP: $x\text{Ce}^{3+}$ increased with the Ce^{3+} concentration; phosphors achieved the highest emission intensity at $x = 0.007$. More dopants will decrease the fluorescent intensity due to concentration quenching. The inset shows that the emission peak position of the phosphors undergoes a certain redshift from 368 nm to 377 nm with the increase in Ce^{3+} concentration, which stems from the fact that Ce^{3+} has a larger ionic radius than Y^{3+} , and the expansion of the local space at elevated concentrations leads to an overall enhancement of the covalency of Ce-O. The centered shift of the 5d level promotes the downward shift of the lowest 5d energy level of Ce^{3+} , i.e., redshift of the emission peaks. The fluorescence spectra of BYP:0.007 Ce^{3+} phosphors are shown in Figure 5b. By monitoring at 370 nm, the excitation spectrum contains a broad band that peaked at 315 nm. The excitation bands ranging from 230 to 340 nm are attributed to partial 4f–5d transitions of Ce^{3+} , pertaining to a lower 5d energy level after splitting in the presence of a crystal field with low C_s symmetry [34]. Under excitation at 315 nm, the BYP: Ce^{3+} phosphor exhibits a broad emission peak around 370 nm. By fitting the emission spectrum with multiple peaks, three curves peaked at 345, 370, and 395 nm can be obtained with good fitness ($R^2 = 99.98\%$). Therein, the emission peak at 395 nm is close to the position of the self-trapped exciton recombination reported in pure BYP crystal [27]. Regarding the double-peak emission of 345 and 370 nm, it may originate from the fact that Ce^{3+} occupied two types of sites, but the energy difference (2225 cm^{-1}) between the two peaks coincides with the general spacing between ${}^2\text{F}_{7/2}$ and ${}^2\text{F}_{5/2}$ levels in Ce^{3+} ($2200\sim 2600\text{ cm}^{-1}$), which verifies the weak CF for Ce^{3+} in the BYP host.

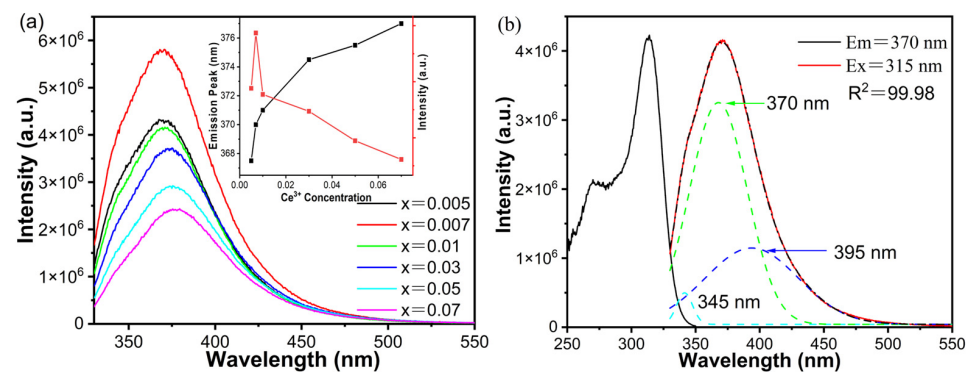


Figure 5. (a) The PL spectra (Ex = 315 nm) of the BYP: $x\text{Ce}^{3+}$ phosphor. The inset graph shows the emission peak wavelength (black) and emission intensities (red) depend on the Ce^{3+} concentration. (b) PLE and PL spectra of the BYP:0.007 Ce^{3+} phosphor.

To further distinguish the emission between the 5d–4f transition of Ce^{3+} and the STE recombination, the low-temperature excitation and temperature-dependent emission spectra of BYP:0.007Ce^{3+} were measured. The PLE spectra of the BYP:0.007Ce^{3+} phosphor measured at 10 K are shown in Figure 6a. The excitation spectra are almost identical when monitored at 345 and 370 nm which implies that the emission related to the two bands originates from the same lowest 5d energy level. The PL spectra of the BYP:0.007Ce^{3+} phosphor measured from 10 to 270 K are shown in Figure 6b. The intensity of the emission peaks at 345 and 370 nm diminishes with increasing temperature, but the peak shapes and peaks are unchanged, which mainly originates from the fact that electrons in the 5d energy level have a higher possibility of thermal activation to the defect levels or conduction band and dissipation due to the assistance of a strong phonon ($1200\text{--}1400\text{ cm}^{-1}$). However, the emission intensities with respect to the 395 nm emission for all samples are almost unaffected, which is generally interpreted as intrinsic luminescence ascribed to the self-trapped excitons and has no relation to the electron population of the lowest Ce-5d energy level. This characteristic emission band has been observed in other orthorhombic phosphate materials like $\text{Ba}_3\text{La}(\text{PO}_4)_3$ and $\text{Ba}_3\text{Lu}(\text{PO}_4)_3$ [27,34], and its larger Stokes shifts, longer emission wavelengths, and broadband emission characteristics are consistent with radiation from self-trapped exciton recombination.

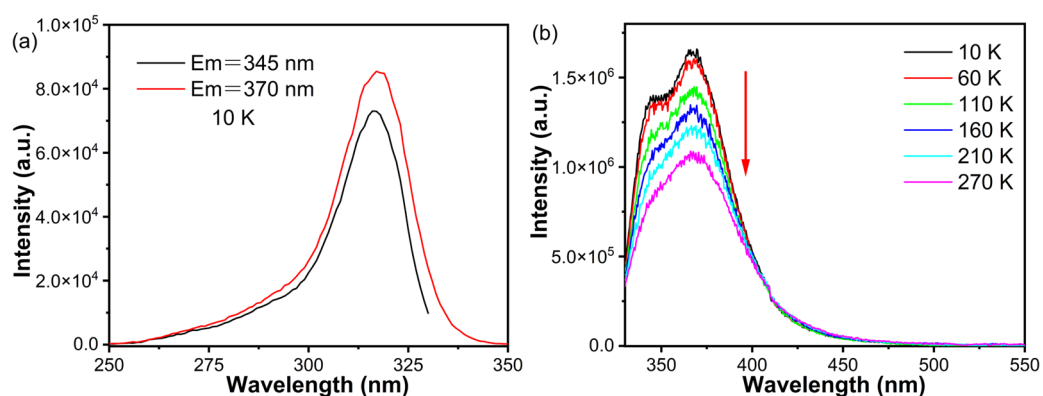


Figure 6. (a) The PLE spectra at 10 K and (b) PL spectra ($\text{Ex} = 315\text{ nm}$) from 10 to 270 K for the BYP:0.007Ce^{3+} phosphor.

3.3. Photo- and Radio-Luminescence Properties of BYP:Ce^{3+} Crystal

At high temperatures, oxygen defects are easily formed in the crystal growth process under an N_2 atmosphere. A crystal wafer in an air atmosphere was annealed for 15 h to minimize the influence of oxygen defects on the properties of the as-grown BYP:Ce^{3+} crystal and compared with the unannealed crystal. The PL spectra of the as-grown and air-annealed BYP:Ce^{3+} crystals were compared and are shown in Figure 7a. Under excitation at 315 nm, the crystal also showed broad emission that peaked at 370 nm. Although the spectral shape of the above two crystal wafers is almost the same, the air-annealed crystal shows an inferior emission intensity, about 2/3 of that of the as-grown crystal. In general, air annealing can reduce thermal stress-induced defects and oxygen vacancies and modify the valence state of cations, but the mechanism of its effect on the fluorescence properties of crystals is somehow complex. The fluorescence decay curves of the as-grown and post-air-annealed BYP:Ce^{3+} crystals are presented in Figure 7b, which can be well fitted by the double-exponential decay equation, and the values are almost the same (average decay lifetime: 17.5 ns vs. 15.5 ns). The fast decay of 8 ns should be attributed to the energy transfer from the $5d_1$ level to STEs, while the latter is closely related to intrinsic defects in the matrix lattice, which have been reported in the radioluminescence of pure BYP crystal [27]. In the present work, the annealing of the crystal did not distinctly change the fluorescence lifetime but significantly decreased the fluorescence intensity. It is suggested that the air-annealing process intensifies the depth of certain trap energy levels, which are

located upside of the 5d lowest energy level of Ce^{3+} , leading to partial trapping of electrons relaxed from the upper levels, reducing the population of the electrons in the 5d lowest level under the same excitation conditions, and thus decreasing the fluorescence intensity, but the radiative transition rates to the 4f ground state would not be affected.

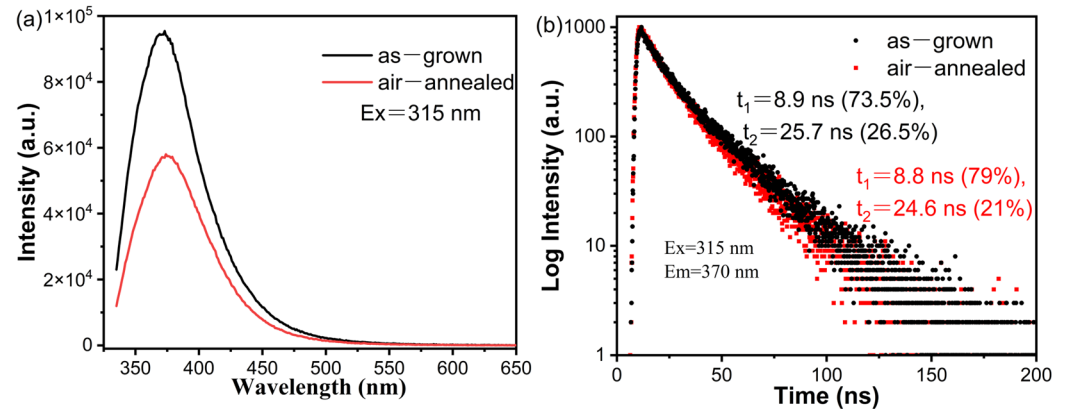


Figure 7. (a) The PL spectra (Ex = 315 nm) of the as-grown and air-annealed crystals and (b) fluorescent decay curves (Ex = 315 nm, Em = 370 nm) of the as-grown and air-annealed $BYP:Ce^{3+}$ crystals.

The X-ray excited luminescent (XEL) spectra of the as-grown and air-annealed $BYP:Ce^{3+}$ crystals are shown in Figure 8a. It is clear that the emission intensity of the air-annealed $BYP:Ce^{3+}$ crystal is significantly weaker than that of the as-grown crystal, and two weak emission peaks around 285 and 305 nm occurred for both of the samples, which are reasonably viewed as the combination of the $5d_2-4f$ transition and color centers, respectively. Upon the disordered occupancy of Ba and Y in the lattice, it is possible for the formation of oxygen vacancies ($Ba'_Y + V_O^{\bullet\bullet} + Ba'_Y$) to maintain the local valence equilibrium, which may in turn trap electrons and become F^+ centers:

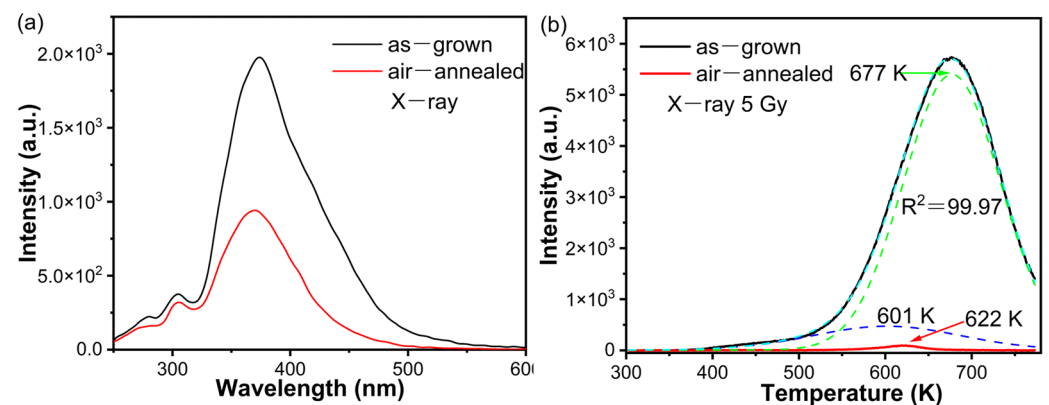


Figure 8. (a) The X-ray excited luminescent spectra and (b) thermoluminescence curves of the as-grown and air-annealed $BYP:Ce^{3+}$ crystals.

A similar phenomenon has been reported in air-annealed Ce^{3+} , Ca^{2+} co-doped $Gd_3Al_2Ga_3O_{12}$ and $(Lu,Y)_2SiO_5$ crystals, etc. [35–38], in which the energy level position of the F^+ center is slightly higher than the $5d_1$ energy level of Ce^{3+} , a position that should be very close to the $5d_2$ energy level and is not easy to detect in PL spectra under excitation at 315 nm. These corresponding emission intensities and peak wavelengths imply that the air-annealing treatment may not be effective in thoroughly eliminating F^+ centers as expected.

The thermoluminescence (TL) spectroscopy of the as-grown and air-annealed BYP:Ce³⁺ crystals was measured for comparison and is shown in Figure 8b. It can be seen that the as-grown crystal exhibits stronger thermoluminescence intensities in the range of 500–770 K with respect to temperature, implying the presence of more shallow or deep trap energy levels. Below 550 K, no thermoluminescence peaks occur in the air-annealed crystal. The TL intensity I vs. temperature T is as follows [39]:

$$I(T) = n_0 S \exp\left(-\frac{E}{kT}\right) \left[(b-1) \left(\frac{S}{\beta}\right) \int_{T_0}^T \exp\left(-\frac{E}{kT}\right) dT + 1 \right] \quad (2)$$

where n_0 is the concentration of trapped charges at $T = 0$; S , E , k , b and β are the frequency factor, depth of the trap, Boltzmann's constant, order of kinetics, heating rate, respectively. This gives the trap depth E as follows [40]:

$$E = T_m [1 + F(S, \beta)] k \log S \quad (3)$$

where the function $f(S, \beta) \ll 1$. For $S \sim 10^9 \text{ s}^{-1}$, the calculation of E (eV) is consistent with the roughly estimated formula $E = T_m/500$ [40,41], where T_m (K) is the peak temperature in the TL curve and the unit of the constant is 500 K/eV. The thermoluminescence peak, corresponding integrated area, and estimated trap depth in the TL glow curves of the as-grown and air-annealed BYP:Ce³⁺ crystals are listed in Table 2. From the comparison of the TL spectra, air annealing indeed reduces most of the thermoluminescence defective energy levels associated with oxygen vacancies, but the shifts of energy levels as well as other non-thermotropic radiative defects with respect to Ba/Y anti-site occupancy in the BYP lattice are still unknown and need to be further investigated.

Table 2. Thermoluminescence peak, corresponding integrated area and trap depth in the TL glow curves of the as-grown and air-annealed BYP:Ce³⁺ crystals.

BYP:Ce Crystal	Temperature/K	Trap Depth E/eV	Intensity/a.u.
as-grown	601	1.202	1.01×10^5
	677	1.354	7.32×10^5
air-annealed	622	1.244	7.25×10^3

3.4. XPS Analysis of BYP:Ce³⁺ Crystal

The survey scan report for the BYP:0.01Ce³⁺ crystal is shown in Figure 9a. The peaks observed in the XPS full spectrum have been found to be related to O, Y, Ba, P and Ce, which ensures the homogeneity of the sample at the atomic level without any other detectable impurities. The high-resolution XPS (HRXPS) spectrum of each element is recorded to determine its valence state. Figure 9b presents a slight asymmetry towards higher binding energy in the HRXPS spectrum of O(1s), which means different types of oxygen species exist in the crystal. The peak is again deconvoluted into two peaks under the best fit that have been positioned at 530.7 and 531.70 eV. The peak observed at lower binding energy is attributed to O 1s (lattice oxygen), while the peak observed at higher binding energy is attributed to V''_O (oxygen vacancies) [42]. The presence of oxygen vacancies in the samples was also preliminarily verified in the PL and TL spectra. The HRXPS spectra of Y (3d), Ba (3d) and P (2p) shown in Figure 9c–e reveal the respective single valence states Y³⁺, Ba²⁺ and P⁵⁺. Also, the HRXPS spectra of Y (3d) and Ba (3d) display doublet peaks corresponding to their states 3d_{5/2} and 3d_{3/2} [43,44]. Figure 9f depicts the HRXPS spectrum of Ce (3d) with a doublet peak allocated at 889.7 eV and 902.5 eV, assigned to states 3d_{5/2} and 3d_{3/2}, respectively. The presence of asymmetry in both peaks towards lower binding energy suggests the existence of Ce in more than one valence state. The peaks are deconvoluted into three peaks under the best fit criteria to identify the valence states of Ce. Deconvoluted peaks are positioned at 885.1 eV, 888.7 and 891.5 eV in 3d_{5/2} and 897.1 eV, 900.9 and 904.4 eV in 3d_{3/2}. The peaks found at binding energies of 885.1,

897.1 and 904.4 eV are assigned to Ce^{3+} , while Ce^{4+} is allocated to the other binding energy values [45].

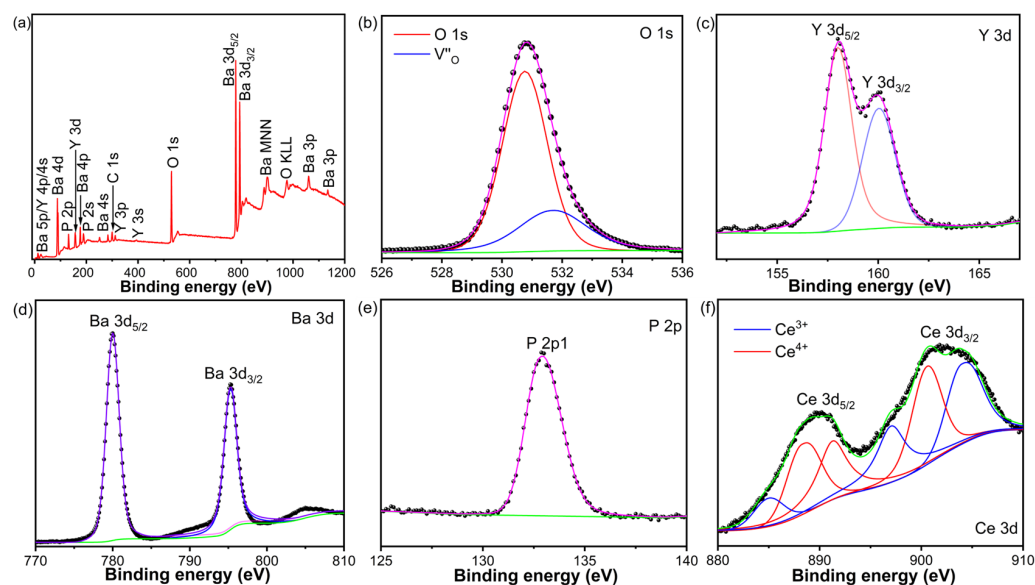


Figure 9. (a) Survey scan report of the BYP: Ce^{3+} crystal and core-level XPS spectra of (b) O 1s, (c) Y 3d, (d) Ba 3d, (e) P 2p and (f) Ce 3d.

4. Conclusions

A transparent scintillation single-crystal BYP with a Ce^{3+} -doping concentration of $x = 0.01$ was first grown by the Cz method and was free of cracks. The XRD patterns confirmed the synthesis of BYP without an impurity phase. The DFT calculation shows its feature of direct-band-gap (5.324 eV) insulators, and the PDOS reveals that both the bottom of the conduction band and the top of the valence band contain components of Ba-5d, Y-3d orbitals, and the band structure should be susceptible to Ba/Y antisite occupancy. The low-temperature fluorescent spectra indicate that the PL emission in the range of 325–500 nm originated from the combination of $5d_1$ – $4f$ transitions of Ce^{3+} and self-trapped excitons. Weak peaks with shorter wavelengths appear in the XEL spectra, which originate from the $5d_2$ energy level and F^+ centers. The air annealing of the BYP: Ce^{3+} crystal significantly reduces the thermoluminescence defects but also reduces the emission intensity under UV or X-ray excitation and fails to remove the possible F^+ centers related to oxygen defects. The presence of oxygen vacancies and Ce^{4+} was confirmed by HRXPS. Impressively, the fluorescence lifetime of the $5d$ level of Ce^{3+} in the BYP crystal is as short as 15.5 ns. The result provides insights into the mechanism of photoluminescence or radioluminescence of Ce^{3+} in eulytite-type phosphate matrices. The Ce^{3+} -doped BYP crystal can be considered a promising candidate for fast scintillators.

Author Contributions: Conceptualization, Z.Z. and G.G.; validation, Z.Z., C.L. and J.Z.; formal analysis, Z.Z., C.L., Y.L., J.Z., Y.S. and J.H.; software, J.W.; investigation, Z.Z., Y.S. and G.G.; data curation, Z.Z. and G.G.; writing—original draft, Z.Z. and G.G.; writing—review and editing, Z.Z., G.G. and H.W. All authors have read and agreed to the published version of the manuscript.

Funding: This work was supported by the National Natural Science Foundation of China (No. 52102004), Jiangxi Provincial Key Research and Development Project of China (No. 20232BBE50030), Jiangxi Province Graduate Innovation Special Fund Project of China (No. YC2022-B182), and Jiangxi Provincial Ganzhou City Key Research and Development Project of China (No. 2022XM079296).

Data Availability Statement: The original contributions presented in the study are included in the article; further inquiries can be directed to the corresponding author.

Acknowledgments: We are greatly grateful to Fulin Lin of the Xiamen Institute of Rare Earths, Chinese Academy of Sciences, for his help in spectroscopic measurement.

Conflicts of Interest: Zhenggang Zou, Yijian Sun, Guoliang Gong, and Herui Wen are employed by the company National Rare Earth Functional Material Innovation Center. The remaining authors declare that the research was conducted in the absence of any commercial or financial relationships that could be construed as potential conflicts of interest.

References

1. Yanagida, T.; Yoshikawa, A.; Yokota, Y.; Kamada, K.; Usuki, Y.; Yamamoto, S.; Miyake, M.; Baba, M.; Kumagai, K.; Sasaki, K.; et al. Development of Pr:LuAG scintillator array and assembly for positron emission mammography. *IEEE Trans. Nucl. Sci.* **2010**, *57*, 1492–1495. [[CrossRef](#)]
2. Michail, C.; Liaparinos, P.; Kalyvas, N.; Kandarakis, I.; Fountos, G.; Valais, I. Phosphors and Scintillators in Biomedical Imaging. *Crystals* **2024**, *14*, 169. [[CrossRef](#)]
3. Alekhin, M.S.; Patton, G.; Dujardin, C.; Douissard, P.A.; Lebugle, M.; Novotny, L.; Stampanoni, M. Stimulated scintillation emission depletion X-ray imaging. *Opt. Express* **2017**, *25*, 654–669. [[CrossRef](#)]
4. Bross, A.D. Applications for large solid scintillator detectors in neutrino and particle astrophysics. *Nucl. Phys. B* **2012**, *229*, 363–367. [[CrossRef](#)]
5. Cieślak, M.J.; Gamage, K.A.A.; Glover, R. Critical Review of Scintillating Crystals for Neutron Detection. *Crystals* **2019**, *9*, 480. [[CrossRef](#)]
6. Yanagida, T.; Fujimoto, Y.; Kurosawa, S.; Kamada, K.; Takahashi, H.; Fukazawa, Y.; Nikl, M.; Chani, V. Temperature dependence of scintillation properties of bright oxide scintillators for well-logging. *Jpn. J. Appl. Phys.* **2013**, *52*, 076401. [[CrossRef](#)]
7. Rodnyi, P.; Dorenbos, P.; Van Eijk, C.W.E. Energy loss in inorganic scintillators. *Phys. Status Solidi B* **1995**, *187*, 15. [[CrossRef](#)]
8. Weber, M. Scintillation: Mechanisms and new crystals. *Nucl. Instrum. Meth. A* **2004**, *527*, 9–14. [[CrossRef](#)]
9. Dorenbos, P. Scintillation mechanisms in Ce³⁺ doped halide scintillators. *Phys. Status Solidi A* **2005**, *202*, 195–200. [[CrossRef](#)]
10. Weber, M.; Derenzo, S.; Moses, W. Measurements of ultrafast scintillation rise times: Evidence of energy transfer mechanisms. *J. Lumin.* **2000**, *87–89*, 830–832. [[CrossRef](#)]
11. Gektin, A.; Korzhik, M. *Inorganic Scintillators for Detector Systems*; Springer: Berlin, Germany, 2005.
12. Nikl, M.; Yoshikawa, A. Recent R&D Trends in Inorganic Single-Crystal Scintillator Materials for Radiation Detection. *Adv. Opt. Mater.* **2015**, *3*, 463–481.
13. Nakauchi, D.; Okada, G.; Kawano, N.; Kawaguchi, N.; Yanagida, T. Luminescent and scintillation properties of Ce-doped Tb₃Al₅O₁₂ crystal grown from Al-rich composition. *Appl. Phys. Exp.* **2017**, *10*, 072601. [[CrossRef](#)]
14. Yanagida, T. Study of rare-earth-doped scintillators. *Opt. Mater.* **2013**, *35*, 1987–1992. [[CrossRef](#)]
15. Wu, G.; Yu, P.; Fan, M.; Chen, F.; Wang, Z.; Cheng, X.; Yu, F.; Zhao, X. Growth and spectroscopic properties of a novel Tm³⁺-doped YSr₃(PO₄)₃ disordered crystal. *J. Lumin.* **2023**, *263*, 119974. [[CrossRef](#)]
16. Rao, L.; Chen, Y.; Huang, J.; Gong, X.; Lin, Y.; Luo, Z.; Huang, Y. Spectroscopic properties and 1.5–1.6 μm laser operation of Er:Yb:Ysr₃(PO₄)₃ crystal. *J. Lumin.* **2022**, *241*, 118441. [[CrossRef](#)]
17. Wu, J.; Huang, J.; Huang, Y.; Gong, X.; Lin, Y.; Luo, Z.; Chen, Y. Continuous-wave and passively Q-switched pulsed 1.5 μm Er:Yb:Ba₃Gd(PO₄)₃ lasers. *Opt. Express* **2022**, *30*, 38848–38855. [[CrossRef](#)]
18. Guo, N.; Lü, W.; Jia, Y.; Lv, W.; Zhao, Q.; You, H. Eu²⁺ & Mn²⁺-Coactivated Ba₃Gd(PO₄)₃ Orange-Yellow-Emitting Phosphor with Tunable Color Tone for UV-Excited White LEDs. *Chem. Phys. Chem.* **2013**, *14*, 192–197.
19. Blasse, G. New Compounds with Eulytine Structure: Crystal Chemistry and Luminescence. *J. Solid State Chem.* **1970**, *2*, 27–30. [[CrossRef](#)]
20. Barbier, J. Structural Refinements of Eulytite-Type Ca₃Bi(PO₄)₃ and Ba₃La(PO₄)₃. *J. Solid State Chem.* **1992**, *101*, 249–256. [[CrossRef](#)]
21. Yang, Z.; Liu, P.; Li, J.; Yang, Q.; Lv, L.; Zhao, Y. A novel yellow luminescent material Ba₃Y(PO₄)₃:Eu²⁺. *J. Alloys Compd.* **2013**, *578*, 118–120. [[CrossRef](#)]
22. Yang, F.; Liu, Y.; Tian, X.; Dong, G.; Yu, Q. Luminescence properties of phosphate phosphor Ba₃Y(PO₄)₃:Sm³⁺. *J. Solid State Chem.* **2015**, *225*, 19–23. [[CrossRef](#)]
23. Li, K.; Liang, S.; Shang, M.; Lian, H.; Lin, J. Photoluminescence and Energy Transfer Properties with Y+SiO₄ Substituting Ba+PO₄ in Ba₃Y(PO₄)₃:Ce³⁺/Tb³⁺, Tb³⁺/Eu³⁺ Phosphors for w-LEDs. *Inorg. Chem.* **2016**, *55*, 7593–7604. [[CrossRef](#)]
24. Liu, Q.; Liu, Y.; Ding, Y.; Peng, Z.; Tian, X.; Yu, Q.; Dong, G. A white light emitting luminescent material Ba₃Y(PO₄)₃:Dy³⁺. *Ceram. Int.* **2014**, *40*, 10125–10129. [[CrossRef](#)]
25. Chen, Y.; Ding, W.; Li, P.; Li, X.; Bao, Q.; Liu, J.; Qiu, K.; Meng, X.; Yang, Z.; Wang, Z. A single-phase white light emitting phosphor Ba₃Y(PO₄)₃:Ce³⁺/Tb³⁺/Mn²⁺: Luminescence, energy transfer and thermal stability. *RSC Adv.* **2019**, *9*, 30406–30418. [[CrossRef](#)]
26. Rajesh, M.; Srinivas, M.; John Sushma, N.; Sanjay Kanna Sharma, T.; Mallikarjuna, K.; Deva Prasad Raju, B. Synthesis and luminescence properties of Pr³⁺ ion-doped Ba₃Y(PO₄)₃ phosphors. *Luminescence* **2021**, *36*, 1991–1996. [[CrossRef](#)] [[PubMed](#)]
27. Takebuchi, Y.; Koshimizu, M.; Ichiba, K.; Kato, T.; Nakauchi, D.; Kawaguchi, N.; Yanagida, T. Scintillation Properties of Ba₃RE(PO₄)₃ Single Crystals (RE = Y, La, Lu). *Materials* **2023**, *16*, 4502. [[CrossRef](#)]

28. Ezawa, H.; Takebuchi, Y.; Ichiba, K.; Kato, T.; Nakauchi, D.; Kawaguchi, N.; Yanagida, T. Evaluation of scintillation and dosimetric properties of undoped and Tb-doped Ba₃Y(PO₄)₃ single crystals. *Opt. Mater.* **2024**, *147*, 114665. [[CrossRef](#)]
29. Segall, M.D.; Lindan, P.J.D.; Probert, M.J.; Pickard, C.J.; Hasnip, P.J.; Clark, S.J.; Payne, M.C. First-principles simulation: Ideas, illustrations and the CASTEP code. *J. Phys. Condens. Matter.* **2002**, *14*, 2717–2744. [[CrossRef](#)]
30. Grau-Crespo, R.; Hamad, S.; Catlow, C.R.A.; de Leeuw, N.H. Symmetry-adapted configurational modelling of fractional site occupancy in solids. *J. Phys. Condens. Matter.* **2007**, *19*, 256201. [[CrossRef](#)]
31. Chakma, U.; Kumer, A.; Al Mashud, A.; Hossain, S.; Alam, M.; Islam, S.; Shaikh, R.; Jony, I.J.; Islam, J. Investigation of electronic structure, optical properties, map of electrostatic potential, and toxicity of HfO₂, Hf_{0.88}Si_{0.12}O₂, Hf_{0.88}Ge_{0.12}O₂ and Hf_{0.88}Sn_{0.12}O₂ by computational and virtual screening. *J. Comput. Electron.* **2023**, *22*, 1–16. [[CrossRef](#)]
32. Lin, L.; Ning, L.; Zhou, R.; Jiang, C.; Peng, M.; Huang, Y.; Chen, J.; Huang, Y.; Tao, Y.; Liang, H. Site Occupation of Eu²⁺ in Ba_{2-x}Sr_xSiO₄ (x = 0–1.9) and Origin of Improved Luminescence Thermal Stability in the Intermediate Composition. *Inorg. Chem.* **2018**, *57*, 7090–7096. [[CrossRef](#)]
33. Kresse, G.; Joubert, D. From ultrasoft pseudopotentials to the projector augmented-wave method. *Phys. Rev. B* **1999**, *59*, 1758–1775. [[CrossRef](#)]
34. Shi, Q.; Huang, Y.; Ivanovskikh, K.V.; Pustovarov, V.A.; Wang, L.; Cui, C.; Huang, P. Luminescence properties and host sensitization study of Ba₃La(PO₄)₃:Ce³⁺ with (V)UV and X-ray excitation. *J. Alloys Compd.* **2020**, *817*, 152704. [[CrossRef](#)]
35. Zheng, R.; Chen, J.; Deng, Y.; Chang, Y.; Liu, Y.; Cheng, R.; Xie, Q.; Xiao, P. Study on the inhomogeneity of LYSO crystal boules grown by the CZ method for PET applications. *J. Cryst. Growth* **2020**, *546*, 125708. [[CrossRef](#)]
36. Nikl, M.; Babin, V.; Pejchal, J.; Laguta, V.V.; Buryi, M.; Mares, J.A.; Kamada, K.; Kurosawa, S.; Yoshikawa, A.; Panek, D.; et al. The Stable Ce⁴⁺ Center: A New Tool to Optimize Ce-Doped Oxide Scintillators. *IEEE Trans. Nucl. Sci.* **2016**, *63*, 433–438. [[CrossRef](#)]
37. Chen, X.; Hu, Z.; Dai, J.; Chen, H.; Shi, Y.; Kou, H.; Wang, T.; Vedda, A.; Beitlerova, A.; Kucerkova, R.; et al. The influence of air annealing on the microstructure and scintillation properties of Ce,Mg:LuAG ceramics. *J. Am. Ceram. Soc.* **2019**, *102*, 1805–1813. [[CrossRef](#)]
38. Dantelle, G.; Boulon, G.; Guyot, Y.; Testemale, D.; Guzik, M.; Kurosawa, S.; Kamada, K.; Yoshikawa, A. Research on Efficient Fast Scintillators: Evidence and X-Ray Absorption Near Edge Spectroscopy Characterization of Ce⁴⁺ in Ce³⁺, Mg²⁺-Co-Doped Gd₃Al₂Ga₃O₁₂ Garnet Crystal. *Phys. Status Solidi B* **2020**, *257*, 1900510. [[CrossRef](#)]
39. Katsumata, T.; Toyomane, S.; Tonegawa, A.; Kanai, Y.; Kaneyama, U.; Shakuno, K.; Sakai, R.; Komuro, S.; Morikawa, T. Characterization of trap levels in long-duration phosphor crystals. *J. Cryst. Growth* **2002**, *361*, 237–239. [[CrossRef](#)]
40. Shalgaonkar, C.; Narlikar, A. A review of the recent methods for determining trap depth from glow curves. *J. Mater. Sci.* **1972**, *7*, 1465–1471.
41. Guo, C.; Tang, Q.; Zhang, C.; Huang, D.; Su, Q. Thermoluminescent properties of Eu²⁺ and RE³⁺ co-doped phosphors CaGa₂S₄: Eu²⁺, RE³⁺ (RE = Ln, excluding Pm, Eu and Lu). *J. Lumin.* **2007**, *126*, 333.
42. Kumar, U.; Padhyay, S.U.; Alvi, P.A. Study of reaction mechanism, structural, optical and oxygen vacancy-controlled luminescence properties of Eu-modified Sr₂SnO₄ Ruddlesden popper oxide. *Physic B* **2021**, *604*, 412708. [[CrossRef](#)]
43. Cole, K.M.; Kirk, D.W.; Thorpe, S.J. Surface Y₂O₃ layer formed on air exposed Y powder characterized by XPS. *Surf. Sci. Spectra* **2020**, *27*, 024010. [[CrossRef](#)]
44. Boukhvalov, D.; Zhidkov, I.; Kukhareenko, A.; Cholakh, S.; Menéndez, J.; Fernández-García, L.; Kurmaev, E. Interaction of graphene oxide with barium titanate in composite: XPS and DFT studies. *J. Alloys Compd.* **2020**, *840*, 155747. [[CrossRef](#)]
45. Paparazzo, E. Use and mis-use of x-ray photoemission spectroscopy Ce3d spectra of Ce₂O₃ and CeO₂. *J. Phys. Condens. Matter* **2020**, *32*, 099501. [[CrossRef](#)]

Disclaimer/Publisher’s Note: The statements, opinions and data contained in all publications are solely those of the individual author(s) and contributor(s) and not of MDPI and/or the editor(s). MDPI and/or the editor(s) disclaim responsibility for any injury to people or property resulting from any ideas, methods, instructions or products referred to in the content.